Chemical Engineering Research and Design 222 (2025) 177–190

Contents lists available at ScienceDirect

Chemical Engineering Research and Design

journal homepage: www.elsevier.com/locate/cherd

A CFD based approach to the modelling of pressure drop and flow pattern evolution through industrial filter systems

Joseph D. Bennett [a],*, Mark C.T. Wilson [b], Nikil Kapur [b], Peter K. Jimack [c], Richard P. Maltby [d], M. Kieran Looney [d]

[a] EPSRC CDT in Fluid Dynamics, University of Leeds, LS2 9JT, UK
[b] School of Mechanical Engineering, University of Leeds, LS2 9JT, UK
[c] School of Computing, University of Leeds, LS2 9JT, UK
[d] Mylar Specialty Films UK Limited, The Wilton Centre, Redcar, TS10 4RF, UK

ARTICLE INFO

MSC:
0000
1111

Keywords:
Polymer melt processes
Filtration modelling
Porous media modelling
Computational fluid dynamics
Industrial filter system evolution

ABSTRACT

A macroscopic CFD approach has been developed to simulate pressure drop and flow pattern evolution in industrial filter systems, specifically for polymer melt filtration in plastic film casting. By coupling filter permeability to local fluid velocity using filter blocking models, the approach avoids direct simulation of particle transport, making it computationally efficient. The model has been validated against a complex real-world filter geometry, accurately capturing pressure drop trends and revealing how flow patterns evolve and filter elements block over time. This approach enables more efficient design and analysis of industrial filtration systems.

1. Introduction

There has been a growing demand for the use of computational methods, such as computational fluid dynamics, to aid in the innovation and understanding of filtration methods in industry (Iliev et al., 2015). Such modelling could lead to the improvement of current filter system designs by homogenising flow distribution around filters, decreasing mean melt residence time and residence time distribution, eliminating dead spots and ultimately improving filter lifetime while allowing for an increase in recycled polymer used in processing.

To computationally model a filtration process in its entirety, a model needs to capture the interaction between the fluid and the filter medium, the transport of solid particles in the fluid, the capture and deposition of solid particles and the interaction between particles in the suspension (Iliev et al., 2015). An added difficulty comes from the fact that all these processes are coupled. Deposited particles in a filter medium act as part of the filter medium itself, changing the geometry at the pore scale. This results in a change in the flow field and the pressure distribution across the filter medium, which in turn influences the transport and deposition of solid particles. The filter medium may also be deformed by the flow field (Iliev et al., 2004). For example, an increased pressure may lead to warping of the filter medium, influencing particle deposition and potentially forcing through already captured particles. The computational cost of simulating such a complicated process over an entire filter system is unrealistic at present (Hrouda et al., 2021).

With computational fluid dynamics (CFD), modelling flow through filtration media can be computationally expensive when refining the mesh to capture pore-scale details while also representing the entire porous medium and surrounding geometry (Teitel, 2010). To address this, macroscopic models are often employed. One widely used approach in CFD is the porous media model (ANSYS Inc, 2012a); it assigns specific properties to a cell zone, referred to as a porous zone, and imposes a pressure penalty as fluid flows through it. Pressure drop through a porous medium may be described by the Forchheimer equation, given by

$$-\Delta P = (\mu/k)u + 0.5C\rho u^2, \tag{1}$$

where ΔP is the pressure drop across the porous medium, μ is the viscosity of the fluid, k is the permeability of the porous medium, u is the velocity of the fluid, C is the Forchheimer coefficient and ρ is the density of the fluid. Inertial effects are negligible when the Reynolds number is less than one and Darcy's law applies (Sidiropoulou et al., 2007), reducing (1) to

$$-\Delta P = (\mu/k)u. \tag{2}$$

---

* Corresponding author.
E-mail address: mm16j2b@leeds.ac.uk (J.D. Bennett).

https://doi.org/10.1016/j.cherd.2025.08.044
Received 8 May 2025; Received in revised form 26 August 2025; Accepted 31 August 2025

Nomenclature

$\boldsymbol{S}$	Source term, N/m^3
$\boldsymbol{u}$	Fluid velocity, m/s
$\boldsymbol{x}$	Position, m
ΔP	Pressure drop, Pa
ΔP^*	Non-dimensional pressure drop
ΔP_0	Initial pressure drop [Pa]
ΔP_{pipe}	Pressure drop across pipe [Pa]
Δt	Time step size [s]
$\dot{\theta}$	Tangential velocity [m/s]
$\dot{\theta}_c$	Central tangential velocity [m/s]
$\dot{\theta}_o$	Outer tangential velocity [m/s]
$\dot{m}$	Mass flow rate, kg/h
$\dot{r}$	Radial velocity [m/s]
$\dot{r}_c$	Central radial velocity [m/s]
$\dot{r}_o$	Outer radial velocity [m/s]
η	Viscous resistance [m^{-2}]
η_0	Initial viscous resistance [m^{-2}]
η_c	Central viscous resistance [m^{-2}]
η_o	Outer viscous resistance [m^{-2}]
$\lvert u \rvert$	Velocity magnitude [m/s]
μ	Viscosity, Pa s
ρ	Density, kg/m^3
ρ_p	Particle density [kg/m^3]
Stk	Stokes number
θ	Angular coordinate [degrees]
θ_c	Central angular coordinate [degrees]
θ_o	Outer angular coordinate [degrees]
A	Cross-sectional area, m^2
C	Forchheimer coefficient
D	Pipe diameter, m
d	Thickness [m]
d_p	Particle diameter [m]
h	Length [m]
k	Permeability, m^2
k_0	Initial permeability [m^2]
K_s	Standard blocking constant [kg^{-1}]
L	Pipe length [m]
l	Characteristic length [m]
P	Pressure, Pa
Q	Volumetric flow rate [m^3/s]
r	Radius/Radial coordinate [m]
r_c	Central radial coordinate [m]
r_c	Outer radial coordinate [m]
T	Temperature, °C
t	Time, s
t_r	Particle relaxation time [s]
u	x-velocity component [m/s]
v	y-velocity component [m/s]
w	z-velocity component [m/s]
x	Distance in the x direction [m]
x_o	Position of outer candle in x direction [m]
y	Distance in the y direction [m]
z	Distance in the z direction [m]
z_o	Position of outer candle in z direction [m]

The porous media model forms the basis of the CFD modelling approach taken in this study; the CFD model of the filter system developed is detailed in Section 2.3.

This study presents a novel methodology for macroscopically modelling filtration in industry scale filter packs. This methodology combines CFD methods and filter blocking models. Filter blocking models are modified to include a coupling between filter permeability and fluid velocity. The model is validated using a complex candle filter pack that is used by Mylar Specialty Films in their film casting process. The filter pack is chosen as data from production runs including the filter pack is used to validate the filtration model. Polyethylene terephthalate (PET) is one of the main polymers used in film production by Mylar Specialty Films (Champion, 2015) and is modelled in this study. Polymer melts are viscoelastic materials, and are classified as non-Newtonian, shear thinning fluids (Denn, 2008). Nevertheless, Bennett et al. (2024) experimentally confirmed that PET melts follow Darcy's law through a range of filter grades and therefore act as Newtonian fluids in filter media.

Fotovati et al. (2012) developed a macroscopic computational model designed to capture the filtration process through pleated filters over time. To save computational cost, particles were released from the inlet in clusters; it was then assumed that clusters deposit fractions of their mass as they travel through the porous medium. Saleh et al. (2014) extended the model to consider polydispersed solid particle loading. Hrouda et al. (2021) developed a novel macroscopic model designed to model filtration processes over time based on a statistical approach using escape probability. The statistical model relates particle diameters to the pore size distribution, which allowed simulations to track if pore spaces are partially or fully blocked as solid particles are filtered.

Basha et al. (2016) used the porous media model and discrete phase modelling to investigate air–oil separation in cartridge filters. As oil droplets deposited over time, the decline in permeability was addressed by updating the inertial and viscous resistances in the porous zone. Computational results showed non-uniform deposition, which was confirmed by experimental observation.

Liu et al. (2019) simulated dust removal and deposition by ceramic candle filters. The filter medium was again represented by a porous zone and to keep computational costs reasonable, particles were grouped into spherical clusters. Particle motion was simulated by considering the drag force on the spherical clusters. Through the CFD model, they were able to find that deposition started at the bottom of the filters before moving upwards. This was verified through comparisons with used filters.

Recently, Lee et al. (2021) modelled the filtration of solid particles from air through a face mask using sequential modelling. A virtual pore-scale model was constructed from μCT images of a mask sample. A porous zone representation of a face mask was generated through three-dimensional scanning. The permeability profile found from the pore scale was implemented into the macroscopic representation of the virtual face mask. Li and Sansalone (2020) coupled a pore-scale filter model with a macroscopic scale sedimentation-filtration model to create a tool for examining particle filtration in radial cartridge filtration. Pore-scale simulations were used to find a filtration coefficient needed for the porous zone CFD model. Lee et al. (2023) used a variety of CFD modelling techniques to model air filtration across filter webs of various scales. A pore-scale model, a parametric model and a porous media model were tested. The parametric model acted as a bridge between the two scales, where the model simplifies the fibrous morphology based on geometrical properties of the fibre material. Modelling methods all suitably predicted the characteristics of filter media tested and were agreeable with experimental data (Lee et al., 2023).

Several mechanistic models have been developed to describe how a filter blocks with particles over time for both pore blocking (depth filtration) and cake filtration (Iritani, 2013). Among them, four standard mechanistic models are used to describe how filters block with particle deposition (Bolton et al., 2006). There is the complete blocking model, the intermediate blocking model, the standard blocking model and cake filtration. These filter blocking models were initially proposed in the context of constant pressure filtration, but have since been reworked to

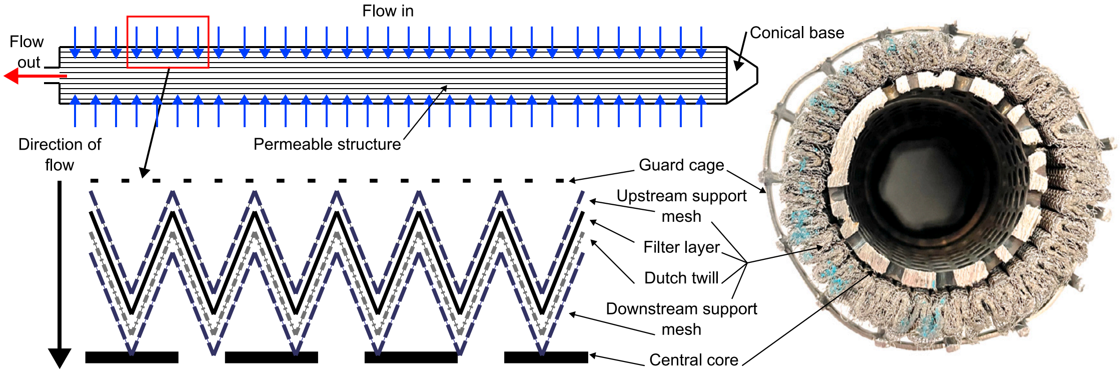

Fig. 1. Sketch and cross-section of a candle filter element.

suit constant rate filtration (Hlavacek and Bouchet, 1993). As constant rate filtration is utilised for film production as a constant flow rate must be maintained to ensure film consistency, the models are considered in this context. The models are all derived from Darcy's law (Bolton et al., 2006).

Each model describes a different pore blocking mechanism (Iritani, 2013). The complete blocking model assumes that each particle completely blocks a single pore. The intermediate blocking model assumes that each particle either partially or fully blocks a pore. The standard blocking model assumes that each particle captured reduces the pore size uniformly, representing depth filtration. The cake filtration model assumes that particles accumulate on top of the filter medium, forming a filter cake.

These models can be used interpret experimental observations (Bolton et al., 2006). Hlavacek and Bouchet (1993) fitted the models to experimental pressure drop evolution curves for constant flow rate filtration of bovine serum albumin (BSA) solutions and found that the intermediate model gave the best fit. Scanning electron micrographs showed the fouling was mainly due to particle surface deposits, showing that the intermediate model was an appropriate choice. Ito et al. (2024) fitted the models to dead-end filtration in bio-process applications. It was found that filtration behaviours differ for different bio-processes and types of filter, hence the suitability of each model changes on a case by case basis. Bowen and Gan (1991) found that in their study, depth filtration was the mechanism of the filtration of BSA through microporous aluminum oxide due to the exceptional fit of the standard model to experimental data, which was confirmed through observation of deposited particles below the surface of used filter samples.

Filter blocking is complex; several mechanisms may combine to simultaneously or consecutively foul a filter (Ito et al., 2024). Combinations of filter blocking models have been described to evaluate situations where several fouling mechanisms occur simultaneously or consecutively, which is frequently observed (Iritani, 2013). Tracey and Davis (1994) found that filter fouling by BSA could be fitted initially by either the complete model or standard model (depending on filter choice) and subsequently by caking, where a layer builds on top of the filter as the pores became constricted. Taghavijeloudar et al. (2019) detailed a model that combined the complete model and cake filtration which gave good agreement to experimental data for the filtration of wastewater sludge. Kirschner et al. (2019) extended blocking models utility to constant flux crossflow filtration and found a combined model of intermediate blocking and cake filtration gave a good fit to experimental data of the filtration of a latex bead suspension. Many combinations of the blocking models have been proposed and are detailed in Iritani (2013). Cheng et al. (2011) developed a general blocking equation based on the Hagen–Poiseuille equation, which summarises the blocking laws which have been proposed in the literature.

Ito et al. (2024) stated that combining models generally give a superior fit to experimental data due to the increased flexibility of an increased number of fitting parameters. This presents an issue with combining models; it is possible that combined models show improved fit not due to an improved physical representation, but rather an increased flexibility due to an increase in number of fitting parameters. Cheng et al. (2011) concluded that simply fitting blocking models to data does not suffice to justify the observed blocking behaviour without assessing the structure of the filter itself. As such, the simpler models should be fitted to experimental data first and the fouling mechanism that each model represents should be considered before any conclusions are drawn. If a simpler model gives a good fit to experimental data and the filtration mechanism they represent is appropriate for the specific application, then it is sufficient in representing the experimental data. If the simpler models all give a poor fit, then combined models should be considered for fitting, as long as the combination of filtration mechanisms represented is logical for the specific application.

Through modification and implementation of the novel filtration model presented in this study, it is possible to use CFD to capture the profiles of pressure evolution data from actual production runs which include industrial filter systems, gain insight into flow pattern evolution inside such filter systems and understand how filters block in such systems over time. The methodology detailed in this study is applicable to a range of actual filter systems in industry.

2. Materials and methods

Before providing detailed exposition of this model, it is necessary to introduce the structure of candle filter elements and the geometry of the seven candle filter pack, which are the subjects of the modelling (and validation) for this study.

2.1. Structure of a candle filter element

Candle filter elements are long (~1 m), thin (~5 cm) cylindrical structures where the filter medium is pleated around a central core. Fig. 1 shows the structure of a candle filter element. A conical, solid base is attached to a cylindrical central core. The heavy duty central core is a thick metal cylinder with holes throughout its structure which allows melt to pass through and is designed to support the filter layer against high pressure gradients during film casting production runs. The filter layer, with a thickness of the order of 1 mm, is pleated around the core and is sandwiched by upstream and downstream support meshes and a Dutch twill layer to add additional protection against high pressure gradients. The filter layer is made of sintered metal fibre and is designed so that 99% of particles of a diameter less than 30 μm are captured. This structure is pleated to maximise filter surface area. The sintered metal fibre used is a depth filtration medium (Porvair Filtration Group Ltd, 2021). Pore diameter varies and some openings may be larger than particles. A thickness of 1 mm is therefore required to

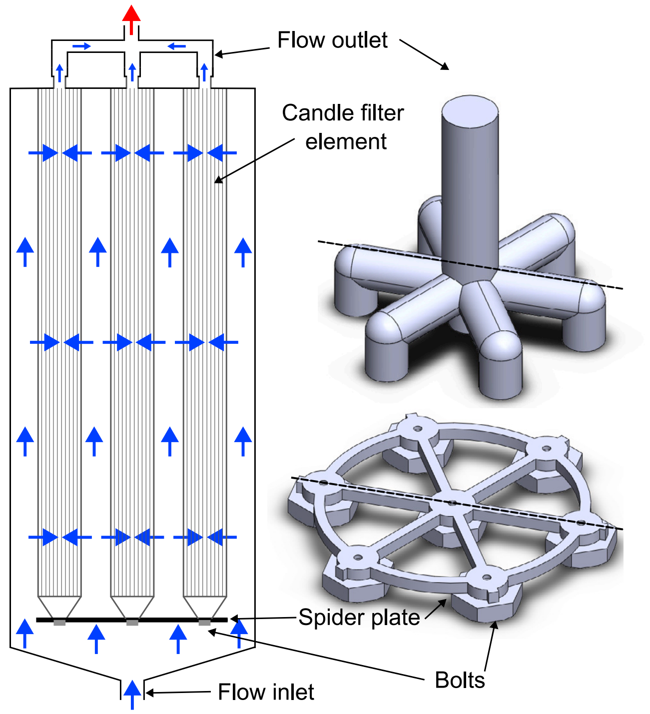

Fig. 2. Cross-sectional sketch of a seven candle filter pack and a 3D model of the spider plate and outlet section. The dashed line through the 3D models shows the position of the cross-sectional sketch.

ensure that particles are deposited within the porous structure. Finally, a guard cage surrounds the pleated filter structure which offers further support. Melt must travel through the guard cage, pleated structure and central core into the central cylinder of the candle. The filtered melt may then escape through the pipe at the top of the candle.

2.2. Filter system geometry

A filter pack consisting of seven candle filter elements is used for filtration in polymer melt processing. Fig. 2 shows a sketch of the seven candle pack and 3D models of the spider plate and the outlet section. A candle filter sits at the centre of the pack. The other six candle filters surround the central candle, with the centre of their bases positioned at the centre of the outer circular structure of the spider plate. The candle filters and spider plate are kept in place with bolts. The spider plate offers mechanical support and helps to distribute the flow between the seven candle filters. Flow travels through the inlet, around the spider plate, and must travel through one of the candle filters to reach the outlet section, onto the next stage of production. At the outlet, the outer six candles have pipes that connect to the central candle outlet.

2.3. Computational model

Fig. 3 shows the computational geometry of the seven candle filter pack that was created in SOLIDWORKS 2019 using CAD drawings of the pack. The origin is placed at the centre of the inlet boundary. All simulations were implemented in ANSYS Fluent 2022 R1. For preliminary analysis, at the inlet, a mass flow rate inlet was specified normal to the boundary and the no-slip condition was specified at the walls. A static pressure outlet was used; the inlet and outlet were extended to be sufficiently far away from the core of the pack, as to have no influence on flow development in the pack. An incompressible, Newtonian fluid was modelled.

A steady, pressure-based solver was selected, and a viscous, incompressible laminar model was applied. In this approach, the Navier–Stokes equations are discretised and solved using the finite volume method. The Navier–Stokes equations for a viscous, Newtonian fluid are given by

$$\begin{gathered}\nabla \cdot \boldsymbol{u} = 0, \\ \rho\left(\frac{\partial \boldsymbol{u}}{\partial t} + \boldsymbol{u} \cdot \nabla \boldsymbol{u}\right) = -\nabla P + \mu \nabla^2 \boldsymbol{u},\end{gathered} \tag{3}$$

where t is time and P is pressure. A coupled pressure-velocity scheme was employed, utilising least squares cell-based gradient discretisation. Second-order discretisation was specified for both pressure and upwind momentum. The solution was initialised using a hybrid method, with the convergence criteria set for maximum scaled residuals on the order of 10^{-5}. Additionally, the pressure drop across the geometry and the mass imbalance between the inlet and outlet were constrained to vary by less than 0.001% per iteration.

The porous media model (ANSYS Inc, 2012b) was used to represent a candle filter element in this model. The porous media model assigns an additional source term in any cell zone where it is enabled, such that

$$\rho\left(\frac{\partial \boldsymbol{u}}{\partial t} + \boldsymbol{u} \cdot \nabla \boldsymbol{u}\right) = -\nabla P + \mu \nabla^2 \boldsymbol{u} + \boldsymbol{S}. \tag{4}$$

This source term accounts for the additional pressure drop due to the resistance imposed on the flow by the porous medium and is given by

$$\boldsymbol{S} = -\left((\mu/k)\boldsymbol{u} + 0.5C\rho|u|\boldsymbol{u}\right). \tag{5}$$

Note that the source term is in the form of the Forchheimer Eq. (1). The Forchheimer coefficient is typically determined using empirical relations, with $C = 0$ when Darcy's law is applicable. Fluent takes viscous resistance (η), the inverse of permeability, as a model input.

2.3.1. The one-twelfth geometry

A 30 degree segment of the geometry, with symmetry boundary conditions, can capture the entirety of the flow through the pack, dramatically reducing computational cost. However, reducing the domain based on symmetry assumes ideal symmetry in geometry, boundary conditions, and flow behaviour. These assumptions can lead to inaccurate results if real-world asymmetries are significant. Bennett (2024) showed that flow through the pack is also symmetrical in the same planes as the geometry. Excellent agreement between the one-twelfth model and a full model was shown. The one-twelfth model contains two porous zones, one-twelfth of the central candle and half of a single outer candle.

2.3.2. Mesh independence

A mesh of the one-twelfth seven candle was created in ANSYS meshing. To ensure sufficient mesh refinement everywhere, the geometry was broken into several sections: the inlet pipe, the geometry around the spider plate and around the candle filters inside the pack, each porous zone, each central core, the outer part, which connects the central core to the outlet pipe, and the outlet. Face sizing was specified at the inlet boundary to ensure sufficient mesh resolution in the inlet section. Sweep meshing was utilised in the inlet pipe, porous zone and outlet pipe as the cross section along the direction of the sweep for these sections is topologically constant. This created a structured, hexahedral mesh. In the central core, outlet part and around the spider plate, mesh was generated with tetrahedra cell shapes, with mesh defeaturing, curvature capture and capture proximity specified. This ensured that the mesh was refined in regions with complicated topology.

The mesh was ensured to be converged with mesh adaptation by analysing the pressure drop across the pack and the total mass flow through porous zones. At the inlet, for the one-twelfth model, a mass flow rate of 0.0625 kg/s was specified (Equivalent to 2700 kg/h for the full geometry). Table 1 shows that the mass flow at the interface

Table 1
Changes in pressure drop across the one-twelfth seven candle pack model and the total mass flow through the sum of each porous zone interface as the mesh is refined through adaptation in regions of high pressure gradients.

Mesh	Mesh elements	Pressure drop [bar]	Total mass flow at interfaces [kg/s]
Original	1,800,000	33.05	0.0567
Adapt 1	3,900,000	33.47	0.0612
Adapt 2	13,400,000	33.75	0.0624
Adapt 3	17,500,000	33.80	0.0624

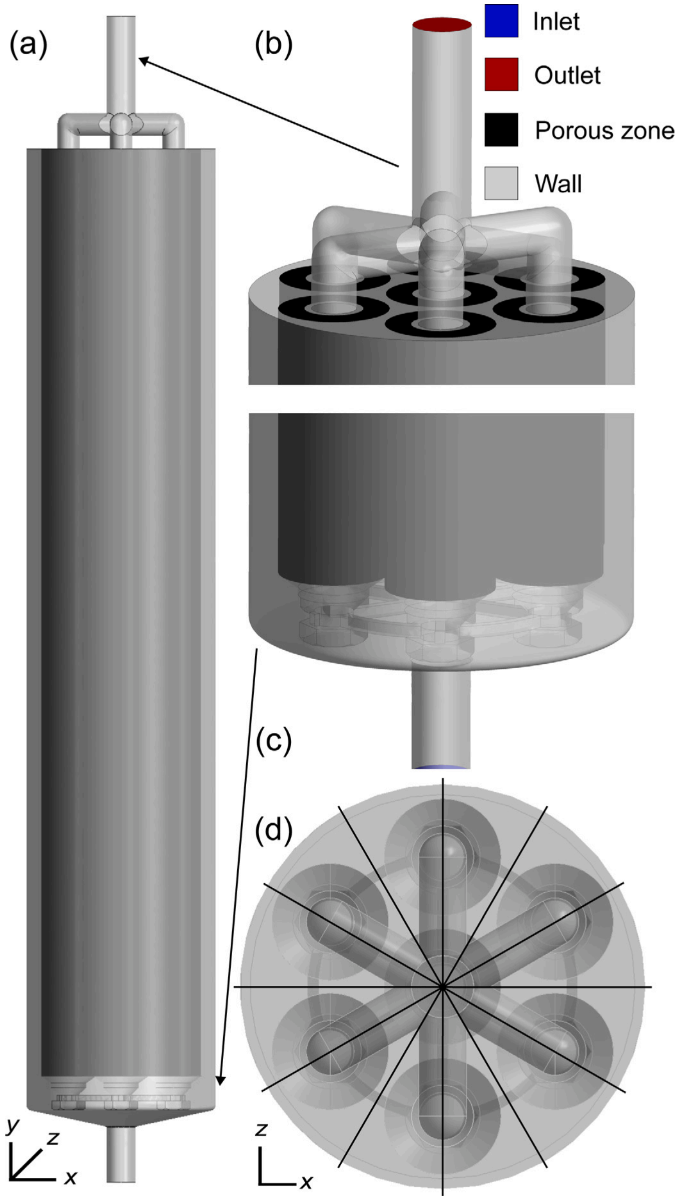

Fig. 3. (a) The seven candle filter pack CFD model. (b) The outlet section. (c) The inlet section. (d) Birdseye view of the filter pack, with planes of symmetry identified. The geometry is modelled using a Cartesian coordinate system, where each point is defined by its x, y and z coordinates.

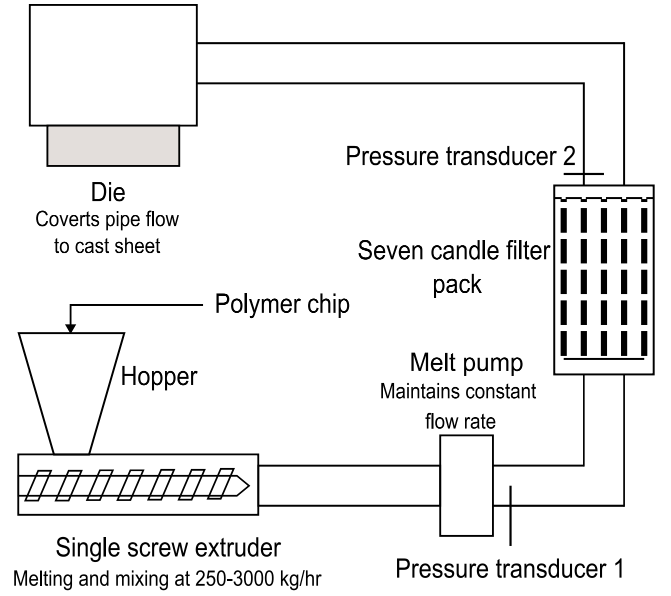

Fig. 4. Sketch of the extrusion system containing the seven candle filter pack.

converges towards the mass flow specified at the inlet with refinement, with the second and third adaptation giving a mass flow through the interface matching that of the inlet.

Table 1 also shows how the pressure drop across the seven candle pack varied with adaptation. Agreement between the second and third adaptation is good, with a 0.15% difference between pressure drop for each mesh. The mesh was deemed to be independent between the second and third adaptation.

3. Filter blocking model

This section describes the novel computational approach that is proposed. We provide details on the analysis of pressure evolution data from production runs of the film casting line with the seven candle filter pack and we describe how filter blocking models are fitted to this data. We describe the methodology developed for macroscopically modelling filtration in industry scale filter systems; the novel filtration model developed is then presented.

3.1. Production run analysis

Data from eight production runs was provided by Mylar for the film production line with a seven candle filter pack. Fig. 4 shows the extruder system on the film casting line with the seven candle filter pack. Two pressure transducers were used to record the pressure and pressure data was recorded every hour. The first pressure transducer is located between the melt pump and the filter pack. The pipe system connecting the pump and filter pack is a straight line pipe. The second transducer sits directly at the outlet of the filter pack. With data from the two pressure transducers, the pressure drop between them is given by $P_1 - P_2$. All runs provided maintained a constant mass flow rate and used the same polymer melt. Throughput for each run was 2700 kg/h. Pipe temperature was set at 290 °C. For this particular PET melt, this gave a density of 1400.1 kg/m^3 and a viscosity of 211 Pa s. Pipe temperature was maintained throughout the extrusion system by a series of heaters and insulation.

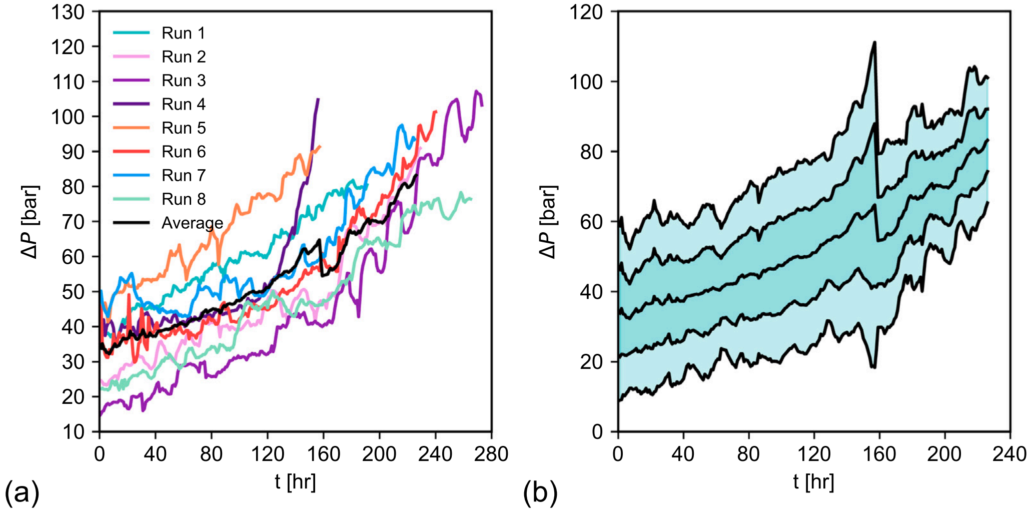

Fig. 5. (a) Pressure drop evolution across the seven candle filter pack for eight production runs. (b) Average pressure drop, with error calculated from the standard deviation of each run from the average.

The Hagen–Poiseuille equation may be used to determine the pressure drop in an incompressible, Newtonian fluid in a laminar regime, through a cylindrical pipe of constant cross section (Pfitzner, 1976). It is given by

$$\Delta P_{\text{pipe}} = \frac{8\mu L Q}{\pi r^4}, \tag{6}$$

where L is pipe length, r is pipe radius and the volumetric flow rate, Q, is given in m^3/s. There is 6.38 m of pipe between pressure transducer 1 and the filter pack inlet. The radius of that pipe is 0.025 m. The volumetric flow rate can be found by converting the mass flow rate to kg/s, then dividing by the density of the melt. Substituting these values into (6), the pressure drop contribution from the pipe between the first transducer and the filter pack is 47.01 bar. Hence, the pressure drop across the filter pack is given by $\Delta P = (P_1 - P_2) - 47.01$.

Fig. 5a shows the pressure drop evolution across the seven candle filter pack for each production run. The average value was computed until 4 of 8 runs were terminated. Fig. 5b shows an error range for the average pressure drop profile, where the smaller error band is taken as the standard deviation from the average and the larger error band is taken from two times the standard deviation from the average. The dip around 160 h is due to the termination of runs 4 and 5, which have a larger pressure drop contribution than other runs and terminate around the same time. Candle filter elements are cleaned and reused. The range of initial pressure drop and differences in pressure drop evolution profiles are therefore likely to be influenced by individual candle element conditions. Differences in pressure evolution profiles are also likely influenced by differences in concentration of blocking particles in each melt. Run 4 and run 5 are terminated before other runs due to the pressure drop exceeding the maximum allowable pressure drop through the extrusion system which triggered an automatic shutdown. This large rate of increase in pressure drop is possibly due to a large concentration of solid particles.

3.2. CFD model calibration

Throughout this study it is assumed that the candle filters are new at the start of production. This means that every candle filter in the seven candle filter pack model initially has a porous zone with the same permeability. This permeability value must be found through calibrating the seven candle pack CFD model, matching its pressure drop output to averaged run data in Fig. 5b. The mass flow rate at the inlet, melt density and melt viscosity of the seven candle pack model were therefore set to match production run conditions, detailed in Section 3.1. In accordance with Darcy's law, the relationship between the reciprocal of permeability and pressure drop was found to be linear (Bennett, 2024). Hence, the calibrated permeability can be found from the linear curve fit. A viscous resistance input of 1.25 $\times 10^9$ m^{-2} was found to give a pressure drop of 33.81 bar across the computational geometry; this is exceptional agreement with the pressure drop of 33.83 bar across the pack from averaged run data. As the agreement between the observed run pressure drop and the seven candle CFD model pressure drop is good, the permeability input for the porous zone of a candle filter element for the CFD models was chosen as 8×10^{-10} m^2 (Bennett, 2024).

3.3. Filter blocking model fit

A filter blocking model may be prescribed to the average seven candle filter pack run data. Bennett (2024) fitted the four simplest models. Complete blocking, standard blocking, intermediate blocking and cake filtration, were fitted and compared. The R^2 values of each fit were compared; the complete model fit gave an R^2 value of 0.937, the cake filtration model fit gave an R^2 value of 0.927, the standard blocking model fit gave an R^2 value of 0.973 and the intermediate blocking model gave an R^2 value of 0.982.

A candle filter layer comprises of a thick, sintered fibre structure, where particles are likely to get captured inside the pores. The manufacturer of candle filters also confirmed that the sintered fibre structure is a depth filtration medium (Porvair Filtration Group Ltd, 2021). The standard model mimics the capture of small particles inside pores. The standard model and intermediate model both gave exceptional fits to the data; the standard model was chosen as the fit is excellent and it is the better physical representation of the filtration mechanism driving particle capture in a sintered fibre material (Bennett, 2024). The standard blocking model is given by

$$\Delta P = \frac{\Delta P_0}{\left(1 - \frac{K_s \dot{m} t}{2}\right)^2}, \tag{7}$$

where ΔP_0 is the initial pressure drop across the filter, $\dot{m}$ is the mass flow rate and K_s is the standard blocking constant. Fig. 6 shows the standard model fit to the run average pressure drop across a filter in the seven candle filter pack.

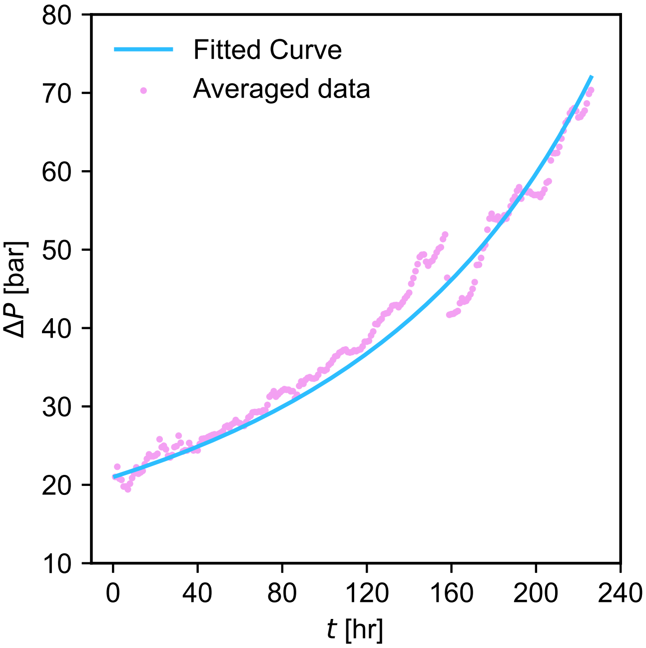

Fig. 6. Standard blocking model fit to the average run pressure drop evolution across a candle element in the seven candle pack.

3.4. Permeability evolution model

Darcy's law (2) may be written as

$$\dot{m} = \frac{\Delta P A \rho k}{d\mu}, \tag{8}$$

where A is the cross-sectional area of the filter and d is the thickness of the filter. Initially, pressure drop across a filter is given by

$$\Delta P_0 = \frac{\dot{m} d\mu}{A\rho k_0}, \tag{9}$$

where k_0 is the initial, clean permeability of the candle filter before any blocking has taken place. Substituting (7) into (8) gives

$$k = \frac{d\mu\dot{m}}{A\rho\Delta P_0}\left(1 - \frac{K_s\dot{m}t}{2}\right)^2. \tag{10}$$

Then, substituting (9) into (10) gives an expression for the permeability evolution using the standard model:

$$k = k_0\left(1 - \frac{K_s\dot{m}t}{2}\right)^2. \tag{11}$$

The Stokes number is a dimensionless number corresponding to the behaviour of particles suspended in a fluid flow (Mujeebu et al., 2009). It is the ratio of characteristic time of a particle to a characteristic time of the flow and is given by

$$\mathrm{Stk} = \frac{t_r|u|}{l}, \tag{12}$$

where t_r is the particle relaxation time and l is a characteristic length. For Stk $\ll 1$, particles will follow streamlines closely (Mujeebu et al., 2009). The particle relaxation time is given by

$$t_r = \frac{\rho_p d_p^2}{18\mu}, \tag{13}$$

where ρ_p is particle density and d_p is particle diameter (Brennen, 2013). Typical dirt particle density is not known. An overcautious maximum particle density is chosen as $\rho_p = 10000$ kg/m^3, which is larger than most metals. An overcautious maximum particle diameter is chosen as $d_p = 1$ mm, the same order as the thickness of the candle filter layer. Melt viscosity modelled will not be lower than 100 Pa s. Hence, a pessimistic upper bound for the particle relaxation time is

$$t_r = \frac{10000 \times 0.001^2}{18 \times 100} < 1 \times 10^{-5}.$$

The seven candle filter pack has a maximum operating throughput of 3000 kg/h and an inlet pipe diameter of $D = 0.03$ m. Hence,

$$\mathrm{Stk} < \frac{1 \times 10^{-5} \times 0.6}{0.03} < 1 \times 10^{-3}$$

and particles follow streamlines in polymer melt flow.

The permeability evolution model (11) is modified to allow the permeability of candle filters to vary based on radial velocity:

$$k(r,\theta,z) = k_0\left(1 - \frac{K_s 2\pi r h\rho\dot{r}(r,\theta,z)t}{2}\right)^2, \tag{14}$$

where h is the length of a candle filter and r and $\dot{r}$ are radial coordinate and radial velocity relative to the centre of the candle filter. The geometry of the model is defined in Cartesian coordinates; however, due to the cylindrical symmetry of the candle filters, analysis is more effectively conducted in cylindrical coordinates, specifically focusing on the radial component. Consider a cylinder of constant radius in the porous zone of a filter pack consisting of a single candle element. By conservation of mass, the mass flow rate through this cylinder must equal that of the mass flow rate specified at the inlet of the filter pack. Taking the mean of (14) at constant r gives

$$\bar{k} = k_0\left(1 - \frac{K_s 2\pi r_d h\rho\bar{\dot{r}}t}{2}\right)^2,$$

where r_d is some constant radius inside the porous zone. But $\bar{\dot{r}} = \frac{\dot{m}}{2\pi r_d h\rho}$ by conservation of mass. Hence, (14) allows the permeability of the candle filter to vary, while recovering (11) on averaging.

Fluent does not use permeability as an input in porous zones. Instead, the viscous resistance must be used. Hence, on implementation in Fluent, (14) is transformed into

$$\eta = \eta_0\left(1 - \frac{K_s 2\pi r h\rho\dot{r}t}{2}\right)^{-2}, \tag{15}$$

where η is the viscous resistance of the porous zone and $\eta_0 = 1/k_0$.

In the one-twelfth geometry, there are two candles, one-twelfth of the central candle and half of an outer candle. Therefore, there are two porous zones; the standard model must be specified for each candle filter. Radial coordinates are employed to examine flow through the central candle, with central radial position denoted as r_c and central radial velocity denoted $\dot{r}_c$. Through the outer candle, radial coordinates are transformed for analysis so that the y-axis is positioned through the centre of the outer candle. The outer radial coordinate is therefore given by

$$r_o = \sqrt{(x - x_o)^2 + (z - z_o)^2}, \tag{16}$$

where (x_o, z_o) is the position of the centre of the outer candle. Therefore, outer radial velocity is found from

$$\dot{r}_o = \frac{(x - x_o)u + (z - z_o)w}{\sqrt{(x - x_o)^2 + (z - z_o)^2}}. \tag{17}$$

For the central candle, the standard model is given by

$$\eta_c = \eta_0\left(1 - K_s\pi r_c h\rho\dot{r}_c t\right)^{-2}, \tag{18}$$

where η_c is the viscous resistance through the central candle. For the outer candle, the standard model assigned is given by

$$\eta_o = \eta_0\left(1 - K_s\pi r_o h\rho\dot{r}_o t\right)^{-2}, \tag{19}$$

where η_o is the viscous resistance through the outer candle.

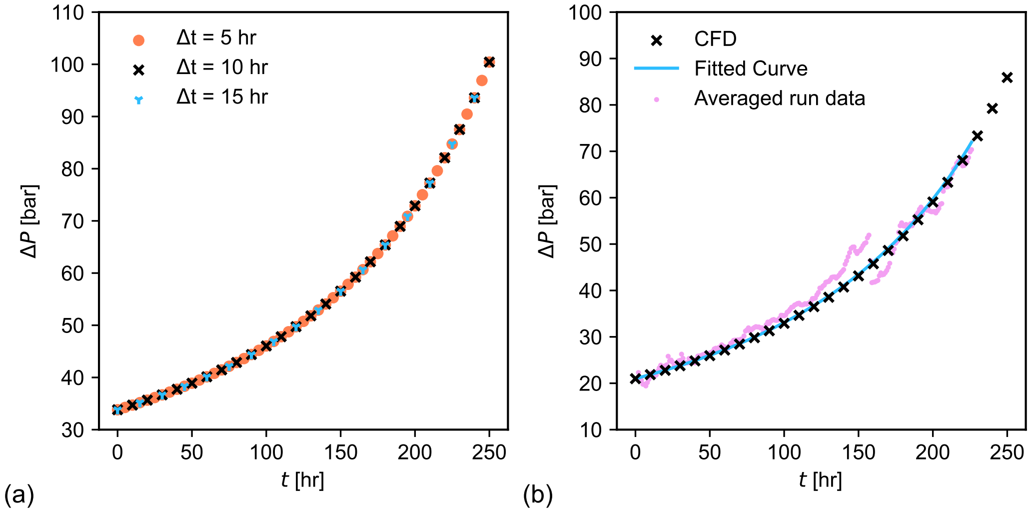

Fig. 7. (a) Pressure drop against time across the filter system for the seven candle filtration model with time steps of 5, 10 and 15 h. (b) Average pressure drop evolution across a candle filter medium inside the seven candle filtration model compared to the standard model curve fitted to the averaged run data.

3.5. Implementation into CFD model

The filtration model (18)–(19) was implemented into the seven candle filter pack CFD model as a series of quasi steady-state simulations. Filter packs block over a period of tens of hours, and production runs last days. Small changes to the flow therefore happen gradually, over several hours. The blocking model couples porous zone viscous resistance and radial velocity. As particles follow streamlines, the local viscous resistance of a filter medium inside the pack depends on the local radial velocity. The velocity must then adapt to changes in the viscous resistance profile, and so on.

User-defined functions (UDFs) were implemented in ANSYS Fluent to model the evolution of viscous resistance and capture local flow properties, enabling dynamic updates of filter behaviour during simulation. These UDFs used custom memory allocations and profiles to control when and how filter properties were updated. The workflow for completion of a successful simulation using UDFs is presented in more detail in Bennett (2024).

4. Results and discussion

Results from the filtration model implemented into the seven candle pack CFD model are presented here. The filtration model is shown to be independent of quasi-steady time step choice. The pressure drop evolution output by the model is compared to the averaged run data. Initial flow patterns through the pack are analysed. Flow pattern evolution is analysed. The filtration model is used to inform on areas of the pack design that may be improved.

Note that each simulation was ensured to converge by ensuring the convergence criteria established in Section 2.3 were met. Appendix A gives an example of convergence for the simulation at $t = 10$ h.

4.1. Time step independence

The quasi-steady state simulations must be independent of time step size. To show this, three time step sizes were tested: 5, 10 and 15 h, within an overall filtration time of 250 h. This exceeds the maximum time of the averaged run data. Fig. 7a shows the pressure drop across the pack from t = 0 h to t = 250 h for simulations using (18)–(19) for the three different time step sizes. The different time steps show matching agreement for pressure drop evolution across the pack. The 10 h time stepping model is used henceforth.

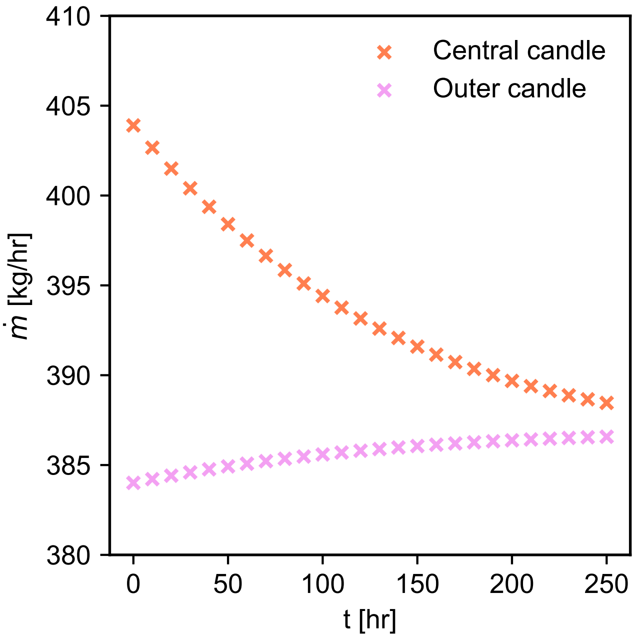

Fig. 8. Mass flow rate through the central and outer candles over time for the seven candle filtration model.

4.2. Model validation

Fig. 7b shows a comparison between the CFD average pressure drop across the filter medium, calculated by averaging the pressure drop across the central and outer porous zones, and the standard model fit to run data given in Fig. 6. The match is exceptional suggesting that the standard blocking model has successfully been implemented into the seven candle filter pack CFD model. This filtration model may therefore be used to offer insight into flow behaviour inside the seven candle filter pack over time.

4.3. Flow pattern analysis

Fig. 8 shows the mass flow rate through the central and outer candles over time. There is significant imbalance in throughput between the central and outer candles initially. This imbalance can be

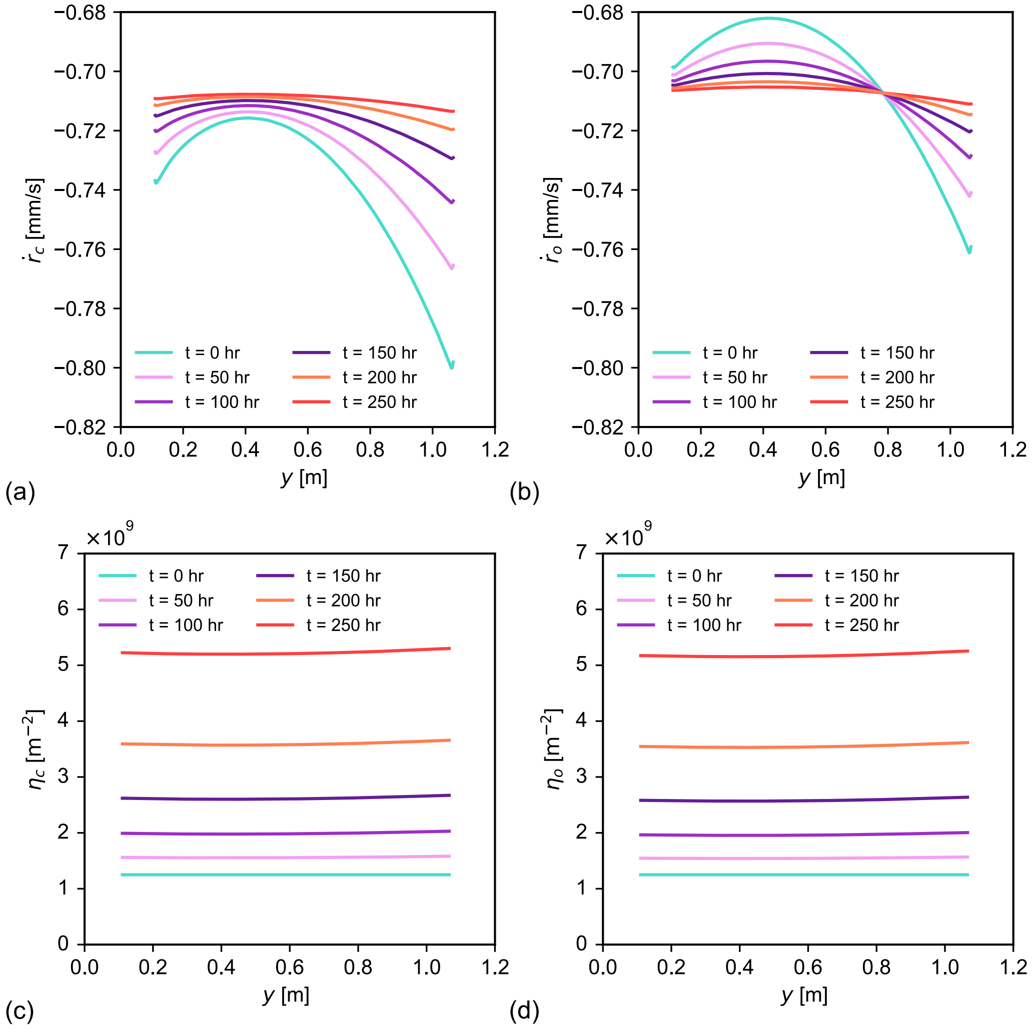

Fig. 9. (a) Central candle radial velocity and (b) outer candle radial velocity against time for the seven candle filtration model along the central and outer candle at a point along $r_c = 0.018$ m and $r_o = 0.018$ m respectively. (c) Central viscous resistance and (d) outer viscous resistance against time for the seven candle filtration model along the central and outer candle at a point along $r_c = 0.018$ m and $r_o = 0.018$ m respectively.

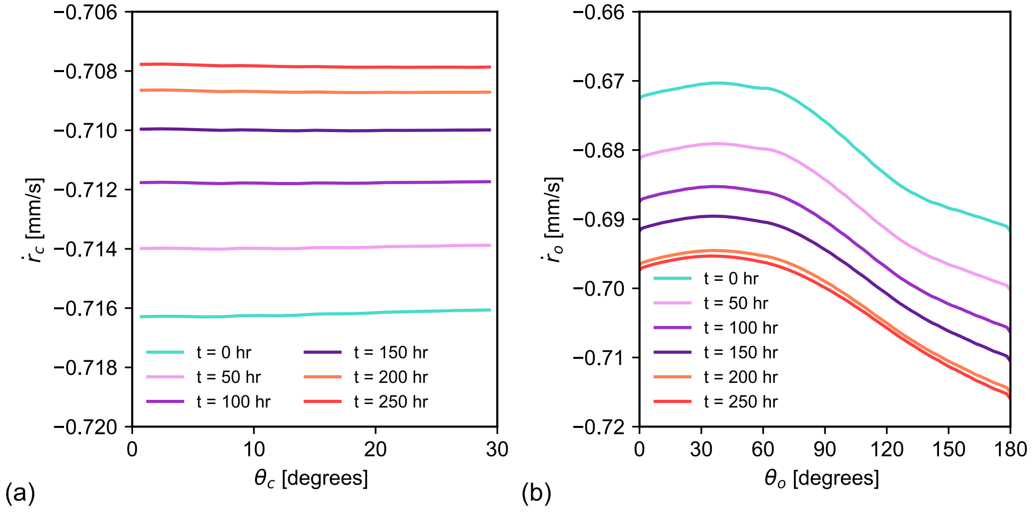

Fig. 10. (a) Central candle radial velocity and (b) outer candle radial velocity against time for the seven candle filtration model around the central and outer candle on the plane $y = 0.45$ m at $r_c = 0.018$ m and $r_o = 0.018$ m respectively.

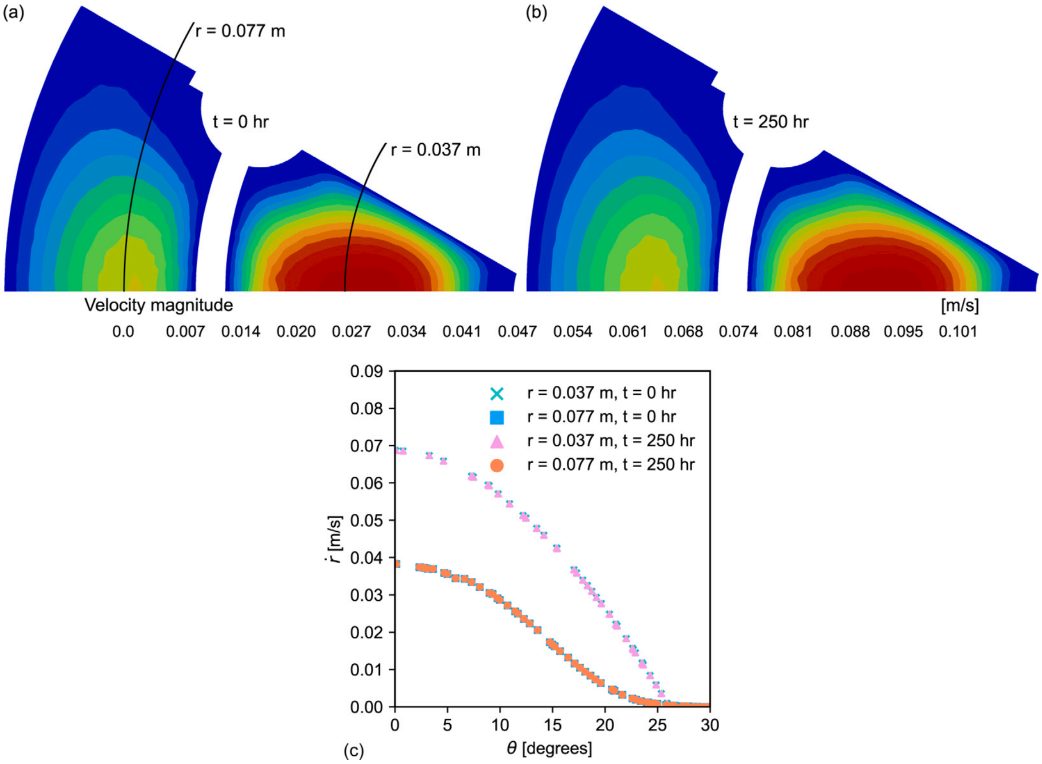

Fig. 11. Contours of velocity magnitude on a plane that cuts through the spider plate for the seven candle filtration model at (a) 0 h and (b) 250 h. (c) Radial velocity along the lines $r = 0.037$ m and $r = 0.077$ m, highlighted in (a), at $t = 0$ and $t = 250$ h.

calculated by the ratio $\dot{m}_c/\dot{m}_o$, where $\dot{m}_c$ is the mass flow rate through the central candle and $\dot{m}_o$ is the mass flow rate each outer candle. A ratio of 1 implies flow is evenly distributed between the central and outer candles, and therefore between all candles in the pack. Initially, $\dot{m}_c/\dot{m}_o = 1.05$; flow is not evenly distributed between candles in the pack. The reason for this difference in distribution is due to the outlet part of the seven candle filter pack; there is additional contribution to the resistance imposed on the flow due to the turn in the outlet section connecting to each outer candle.

Over time, mass flow through the central candle decreases and mass flow through the outer candle increases. Both appear to be converging towards an even proportion of flow through each candle. As the central candle sees more flow (and therefore more particles), the average viscous resistance through it will increase at a faster rate compared to the outer candle. The flow will redistribute in response to this. By multiplying the mass flow rate at each point in Fig. 8 by ten (due to the 10 h time step size) and summing, the total mass flow through each filter after 250 h can be estimated. The central candle has seen 102 450 kg of melt compared to 100 270 kg of melt seen by each outer candle. The imbalance in mass flow rate between the central and each outer candle filter has reduced to $\dot{m}_c/\dot{m}_o = 1.01$ after 250 h.

Fig. 9a–b shows the central and outer radial velocity through a line along the central and outer candle respectively. Initially, as the fluid moves up the pack, there is clear variation in central radial velocity and outer radial velocity. Central radial velocity is greater in magnitude along the candle as the central candle sees a greater proportion of the total throughput. As time advances, the flow appears to be converging towards a uniform ‘box’ profile along the candle filters. Furthermore, the central radial velocity is decreasing in magnitude as time advances. The mean central radial velocity has decreased significantly compared to a slight increase in mean outer radial velocity. As the distribution of melt flow between candle filters homogenises, the mass flow rate through the central candle redistributes through the six outer candles, significantly reducing the central radial velocity along the central candle, while slightly increasing outer radial velocity along each outer candle. Fig. 9c–d shows the central and outer viscous resistance profiles along the same line along each candle filter. The mean viscous resistance through the central candle is 5.23×10^{10} m^{-2}, around 1% larger than the 5.18×10^{10} m^{-2} through the outer candle after 250 h. This is because the central candle has seen a greater throughput, leading to more blocking, resulting in a larger resistance to the flow.

Fig. 10 shows radial velocity plotted along $r_c = 0.018$ m for the central candle and outer radial velocity along $r_o = 0.018$ m for the outer candle on the plane $y = 0.45$ m. Initially, there is little variation around θ_c, the angular coordinate relative to the central candle, for the chosen radii in the central candle, suggesting flow is independent of θ_c. Through the outer candle, there is significant variation in outer radial velocity for the chosen radii, indicating that the flow is dependent on θ_o, the angular coordinate relative to the outer candle. Fig. 10 also shows the central and outer radial velocity evolution around constant r_c and r_o respectively. The magnitude of central radial velocity has decreased around the central filter and the magnitude of the outer radial velocity has increased around the outer filter. There is little change in radial velocity profiles around the candle filters on this plane. It does not appear that the blocking model is homogenising flow around the outer filter.

As time advances and the candle filters block, flow between and (vertically) along candle filters in the seven candle filter pack homogenise. Fig. 11a–b shows contours of velocity magnitude through the spider plate at 0 and 250 h. There is no qualitative difference in the two contours plots at the spider plate over the course of blocking model simulations. Fig. 11c show radial velocity profiles along lines of constant r highlighted in Fig. 11a. There is no discernible difference in radial velocity along the lines; filter blocking has negligible influence on the flow around and upstream of the spider plate.

Fig. 12 shows contours and vectors of velocity magnitude through a plane that cuts through the middle section of the seven candle filter pack at 0 and 250 h. Flow patterns are structurally similar at each time. Flow patterns do not change significantly as demonstrated by the negligible change to radial velocity profiles around each candle filter.

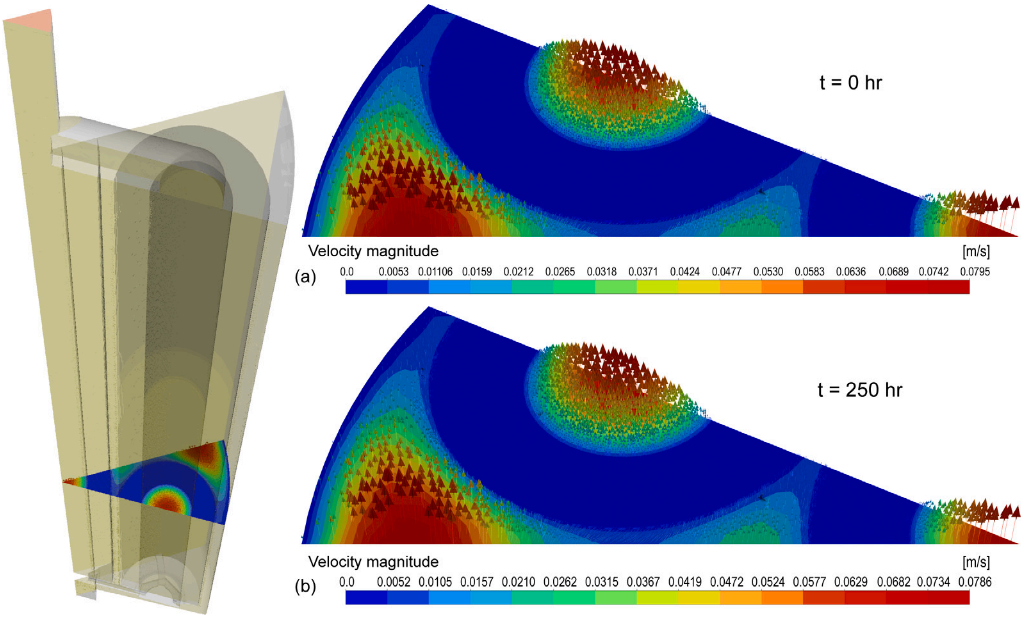

Fig. 12. Contours and vectors of velocity magnitude for the seven candle filtration model at $y = 0.45$ m at (a) 0 h and (b) 250 h.

Appendix B details a parameter study, where operating throughput and melt viscosity were varied. It shows that homogenisation along and between filters over the course of a run in the seven candle filter pack was superior when operating at as large a flow rate as possible.

In summary, the standard blocking model has been successfully implemented into the seven candle filter pack CFD model, with results remaining stable beyond the maximum time of the averaged run data. As time advances, flow *between* and *along* candle filters in the pack homogenise. Flow *around* the outer candle filter does not appear to homogenise as time advances.

Ideally, the distribution of throughput between candles would be homogenised. Candles are cleaned and reused after the termination of a run. If the flow is not homogenised, some candles in the pack would block at a faster rate compared to others, increasing pressure drop across the candles which see more throughput. It is therefore recommended that each of the seven candles is rotated over the course of seven production runs, where a different candle element is placed at the centre of the pack for each run.

5. Conclusion

This work details the creation of a novel filtration model, which modified a common filter blocking model to include dependence on local radial velocity, and its implementation into a CFD model of an industrial filter system. Through modification and implementation of the filtration model into the CFD model of a filter system, it was possible to capture the profiles of averaged pressure evolution data from actual runs, gain insight into flow pattern evolution through the system and understand how filters in the system block over time.

The filtration model showed that issues with the original design of the filter system caused imbalance in the flow rate split between filter elements. We suggest that the model is used to address this imbalance. The flow outlet should be redesigned to ensure that the path through each candle imposes equal resistance to the flow. The filtration model may then be used with the modified flow outlet to ensure even flow distribution over the course of a production run for a range of operating parameters. This would ensure that the flow does not favour the central candle. This ensures that the filter pack will perform better with a more even flow distribution between the candles at lower throughputs and pressure drops across the pack. This shows a powerful application of the model; it may be used optimise industrial standard filter system design, which may extend filter element lifetime and reduce system shutdowns, ultimately saving production costs.

The coupling between modified filter blocking models and CFD models to predict pressure drop evolution, filter blocking evolution and flow pattern evolution across a geometrically complex filter system on a macroscopic scale has been shown to work for a complex 3D CFD model. The framework detailed in this work is applicable to a range of actual filter systems in industry wherever certain physical requirements are satisfied. The fluid must act as a Newtonian fluid throughout the pack. Furthermore, Darcy's law must apply to the fluid as it flows through the filter medium. Finally, the model is based upon the assumption that particles follow streamlines of the flow (i.e. a low Stokes number regime). Therefore, to model polymer melt filtration, it is a requirement that the polymer melt acts as a Newtonian fluid under the filtration operational conditions. Conversely, the framework may be used to model any Newtonian fluid that obeys Darcy's law. Hence, this framework is not limited to modelling polymer melts. For example, viscous flow filtration is utilised in the pharmaceutical and chemical industries (Hanspal et al., 2006).

The appropriate filter blocking law should also be chosen; in the case of the candle filter system analysed in this study, the standard blocking model was chosen as it gave a good fit to average run data and it was defined based on the same physical particle deposition mechanism that drives particle deposition in candle filter media. Future work could involve using different blocking models (to represent different physical filtration properties) or application of the filtration model to test modifications to the geometry of a seven candle pack to improve flow distribution.

The CFD model was validated against averaged production run data. Further experimental work could be undertaken to collect experimental data under controlled conditions to further refine the flow paths and conditions predicted by the CFD model. However, this would be a difficult task due to the inaccessible nature of industrial scale filtration systems and the extreme operating conditions associated with polymer melt filtration.

CRediT authorship contribution statement

Joseph D. Bennett: Writing – review & editing, Writing – original draft, Visualization, Validation, Methodology, Investigation, Funding acquisition, Formal analysis, Data curation, Conceptualization. **Mark**

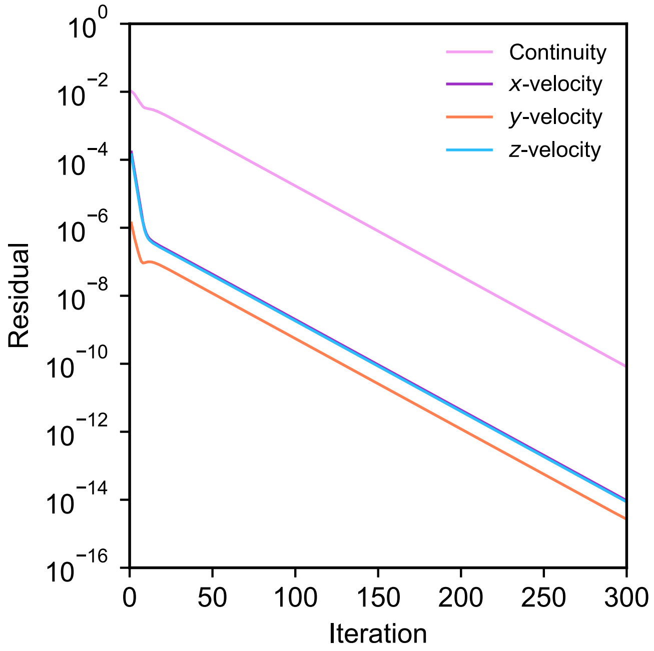

Fig. A.1. Scaled residuals against number of iterations for the seven candle filtration model at $t = 10$ h.

C.T. Wilson: Writing – review & editing, Supervision, Conceptualization. **Nikil Kapur:** Writing – review & editing, Supervision, Conceptualization. **Peter K. Jimack:** Writing – review & editing, Supervision, Conceptualization. **Richard P. Maltby:** Writing – review & editing, Supervision, Resources, Conceptualization. **M. Kieran Looney:** Writing – review & editing, Resources, Conceptualization.

Declaration of competing interest

The authors declare that they have no known competing financial interests or personal relationships that could have appeared to influence the work reported in this paper.

Acknowledgements

This work was supported by the Engineering and Physical Sciences Research Council (EPSRC), Centre for Doctoral Training in Fluid Dynamics. This work was also supported by Mylar Specialty Films. For the purpose of open access, the author has applied a Creative Commons Attribution (CC BY) licence to any Author Accepted Manuscript version arising from this submission.

Appendix A. Convergence

Fig. A.1 shows a plot of the scaled residuals against the number of iterations for the simulation at time $t = 10$ h. All residuals are less than the convergence criteria set for maximum scaled residuals on the order of 10^{-5}.

Fig. A.2 shows the pressure drop across the geometry and the mass imbalance between the inlet and outlet against the number of iterations. Both parameters varied by less than 0.001% per iteration. Hence, the simulation was sufficiently resolved. The same convergence criteria were ensured to be met for all simulations.

Table B.1
Values of viscosity, mass flow rate and Reynolds number for seven different tests with the seven candle pack.

Test number	$\dot{m}$ [kg/h]	μ [Pa s]	Re
1	250	400	0.0074
2	937.5	330	0.0335
3	1625	260	0.0737
4	2312.5	190	0.1435
5	3000	120	0.2947
6	250	120	0.0245
7	3000	400	0.0884

Table B.2
Initial distribution of flow between the central and outer candle for each test.

Test number	Central flow distribution [%]	Outer flow distribution [%]
1	51.26	48.74
2	51.26	48.74
3	51.26	48.74
4	51.26	48.74
5	51.26	48.74
6	51.26	48.74
7	51.26	48.74

Appendix B. Parametric analysis

The production line with the modelled filter system operates over a large range of throughputs and temperatures. This Appendix uses the filter blocking model to explore the influence of melt viscosity and throughput on pressure drop and flow pattern evolution.

Seven tests were undertaken, designed to explore the extent of the range and combinations of melt viscosity and pumped throughput for the film casting process. Table B.1 shows the melt viscosity and throughput selected for each test. The standard fitting parameter K_s was identical throughout all the tests.

Fig. B.1a shows pressure drop evolution across the pack for each test. Fig. B.1b shows a comparison of non-dimensionalised pressure drop evolution between each test. That is

$$\Delta P^* = \frac{\Delta P}{\Delta P_0},$$

where ΔP^* is the non-dimensionalised pressure drop and ΔP_0 is the initial pressure drop across the pack ($t = 0$). For tests with matching flow rates, such as tests 5 and 7, non-dimensional pressure drop evolution matches. It is clear from Fig. B.1a that the rate of increase of pressure evolution is larger for test 7 compared to test 5. Hence, initial pressure drop across the pack and rate of pressure drop evolution scale with viscosity. Fig. B.1b also shows that the rate of pressure drop evolution scales with flow rate. Furthermore, from tests 1 and 6 in Fig. B.1a, which have the same viscosity, initial pressure drop differs. Hence initial pressure drop scales with throughput, which is consistent with Darcy's law.

Table B.2 shows the initial percentage split of total mass flow rate between the whole central and an outer candle for each test. Melt viscosity and throughput have no influence on the distribution of flow between each candle initially. This is because these parameters do not contribute to the initial resistance on the flow imposed by the candle filters. Furthermore, the Reynolds number for all tests remains in the creeping flow regime. This suggests that flow through the pack is dynamically similar over the range of operating throughputs and melt viscosities. Bennett (2024) shows that the flow is initially dynamically similar regardless of melt viscosity and throughput.

Table B.3 shows the percentage split of mass flow between the central and outer candles for each test after 200 h. The distribution through all tests has changed and is converging towards an even split between central and outer candles. The tests with a larger operating throughput see a more even distribution between each candle after

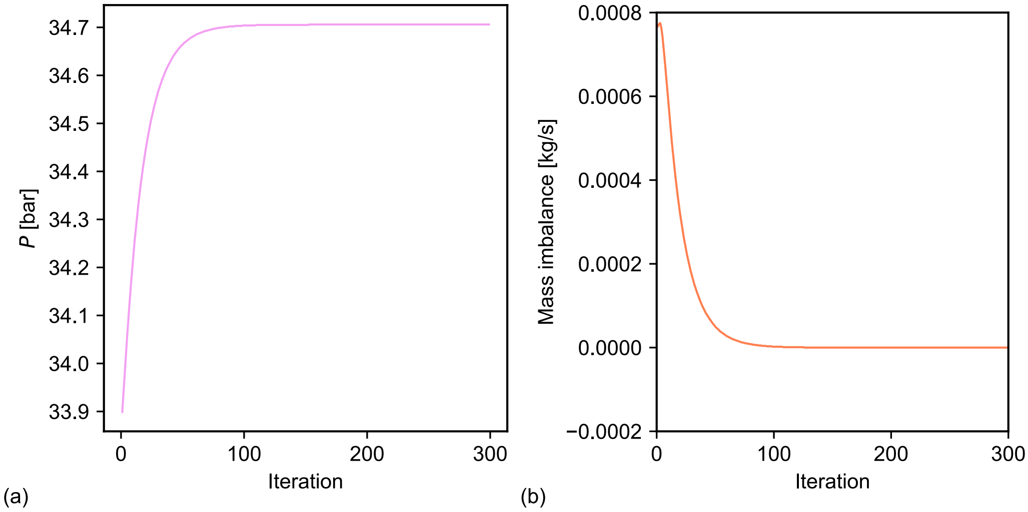

Fig. A.2. (a) Pressure drop across the filter system and (b) mass flow rate imbalance between the inlet and outlet against number of iterations for the seven candle filtration model at t = 10 h.

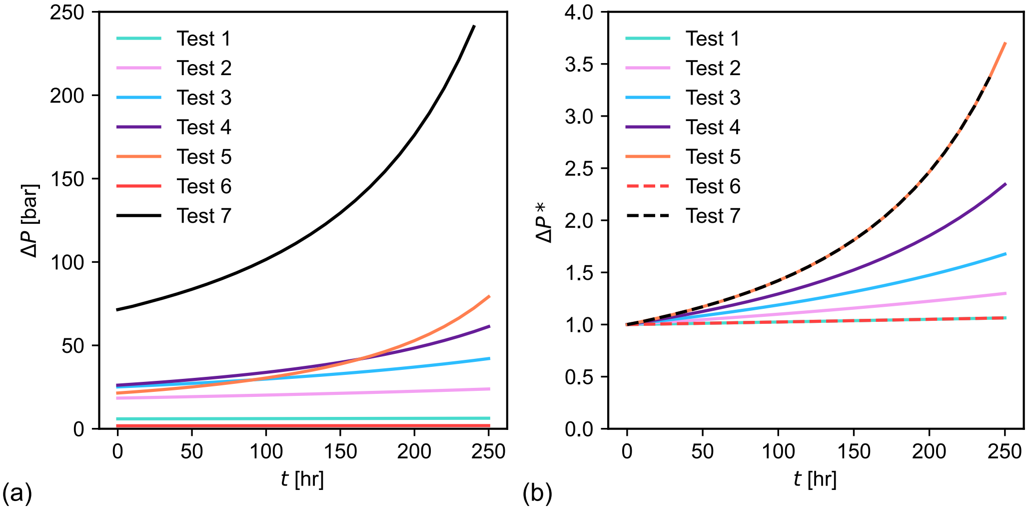

Fig. B.1. (a) Pressure drop evolution across the filter pack for the seven tests described in Table B.1. (b) Non-dimensionalised pressure drop against time across the filter system for each test.

Table B.3
Distribution of flow between the central and outer candle for each parameter test after 200 h.

Test number	Central flow distribution [%]	Outer flow distribution [%]
1	51.11	48.89
2	50.75	49.25
3	50.48	49.52
4	50.29	49.71
5	50.17	49.83
6	51.11	48.89
7	50.17	49.83

200 h. The larger the operating throughput, the more cumulative throughput of melt through each candle filter, the faster the distribution converges towards an even split. Tests 1 and 6 have the same distribution between candle filters after 200 h. These tests have the same operating throughput, but different melt viscosities. The same is true for tests 5 and 7. This suggests that viscosity has little influence on flow distribution evolution for the materials and temperature ranges of interest. Bennett (2024) shows that viscosity has no influence on flow patterns throughout the pack.

In summary, the initial pressure drop across the pack and the rate of pressure drop evolution are dependent on both melt viscosity and operating throughput. Viscosity has no influence on flow patterns through the pack. Flow patterns are initially dynamically similar over the range of operating throughputs through the seven candle filter pack; operating throughput dictates the magnitude of velocity of the flow and viscosity has no influence. The choice of melt viscosity will only change the work needed from the pump to maintain a desired operating throughput.

References

ANSYS Inc, 2012a. ANSYS FLUENT 12.0/12.1 Documentation. ANSYS, Inc, Canonsburg, Pennsylvania, United States.

ANSYS Inc, 2012b. ANSYS FLUENT 12.0 user's guide - 7.2.3 porous media conditions.

Basha, N., Cochrane, L., Culham, S., Hamad, F., Ali, Z., 2016. CFD study of filtration process in moulded filters within a vacuum pump. In: FILTECH. FILTECH, pp. 1–10.

Bennett, J.D., 2024. Fluid Mechanics of Polymer Melt Filtration (Ph.D. thesis). University of Leeds, Leeds.

Bennett, J.D., Wilson, M.C., Kapur, N., Jimack, P.K., Maltby, R.P., Looney, M.K., 2024. Computational modelling and experimental validation of pressure drop through multi-layered woven screens for polymer melts. Chem. Eng. Res. Des. 209, 323–333. http://dx.doi.org/10.1016/J.CHERD.2024.08.002.

Bolton, G., LaCasse, D., Kuriyel, R., 2006. Combined models of membrane fouling: Development and application to microfiltration and ultrafiltration of biological fluids. J. Membr. Sci. 277, 75–84.

Bowen, W.R., Gan, Q., 1991. Properties of microfiltration membranes: flux loss during constant pressure permeation of bovine serum albumin. Biotechnol. Bioeng. 38 (7), 688–696. http://dx.doi.org/10.1002/BIT.260380703.

Brennen, C.E., 2013. Fundamentals of multiphase flow. Fundam. Multiph. Flow 9780521848046, 1–345. http://dx.doi.org/10.1017/CBO9780511807169.

Champion, J., 2015. Use of Computational Fluid Dynamics to Improve the Layer Thickness Control of Polyester Based Multilayered Films (Ph.D. thesis). University of Birmingham, Birmingham.

Cheng, Y.L., Lee, D.J., Lai, J.Y., 2011. Filtration blocking laws: Revisited. J. Taiwan Inst. Chem. Eng. 42 (3), 506–508. http://dx.doi.org/10.1016/J.JTICE.2010.09.004.

Denn, M.M., 2008. Polymer Melt Processing: Foundations in Fluid Mechanics and Heat Transfer. Cambridge University Press.

Fotovati, S., Tafreshi, H.V., Pourdeyhimi, B., 2012. A macroscale model for simulating pressure drop and collection efficiency of pleated filters over time. Sep. Purif. Technol. 98, 344–355. http://dx.doi.org/10.1016/j.seppur.2012.07.009.

Hanspal, N.S., Waghode, A.N., Nassehi, V., Wakeman, R.J., 2006. Numerical analysis of coupled Stokes/Darcy flows in industrial filtrations. Transp. Porous Media 64 (1), 73–101. http://dx.doi.org/10.1007/S11242-005-1457-3/METRICS, URL https://link.springer.com/article/10.1007/s11242-005-1457-3.

Hlavacek, M., Bouchet, F., 1993. Constant flowrate blocking laws and an example of their application to dead-end microfiltration of protein solutions. J. Membr. Sci. 82, 285–295.

Hrouda, A., Capek, L., Vanierschot, M., Denis, K., 2021. Macroscale simulation of the filtration process of porous media based on statistical capturing models. Sep. Purif. Technol. 266, http://dx.doi.org/10.1016/j.seppur.2021.118577.

Iliev, O., Kirsch, R., Lakdawala, Z., Rief, S., Steiner, K., 2015. Modeling and simulation of filtration processes. In: Currents in Industrial Mathematics: From Concepts to Research to Education. Springer Berlin Heidelberg, pp. 163–228.

Iliev, O., Mikelic, A., Popov, P., 2004. Fluid Structure Interaction Problems in Deformable Porous Media: Toward Permeability of Deformable Porous Media. Tech. Rep., Fraunhofer-Institut für Techno- und Wirtschaftsmathematik.

Iritani, E., 2013. A review on modeling of pore-blocking behaviors of membranes during pressurized membrane filtration. http://dx.doi.org/10.1080/07373937.2012.683123.

Ito, T., Liao, X., Lee, S., Hanada, T., 2024. Implementation of filtration models for filter performance prediction in bioprocess dead-end membrane filtration. Biochem. Eng. J. 208, 109358. http://dx.doi.org/10.1016/J.BEJ.2024.109358.

Kirschner, A.Y., Cheng, Y.H., Paul, D.R., Field, R.W., Freeman, B.D., 2019. Fouling mechanisms in constant flux crossflow ultrafiltration. J. Membr. Sci. 574, 65–75. http://dx.doi.org/10.1016/J.MEMSCI.2018.12.001.

Lee, K., Jung, Y.W., Park, H., Kim, D., Kim, J., 2021. Sequential multiscale simulation of a filtering facepiece for prediction of filtration efficiency and resistance in varied particulate scenarios. ACS Appl. Mater. Interfaces 13 (48), 57908–57920. http://dx.doi.org/10.1021/acsami.1c16850.

Lee, K., Kim, D., Kim, J., 2023. Computational modeling of multiscale air filter media consisting of nano- and microfibers. ACS Appl. Nano Mater. 6 (11), 9415–9425. http://dx.doi.org/10.1021/acsanm.3c01139.

Li, H., Sansalone, J., 2020. Multi-scale physical model simulation of particle filtration using computational fluid dynamics. J. Environ. Manag. 271, 111021. http://dx.doi.org/10.1016/J.JENVMAN.2020.111021.

Liu, K., Zhao, Y., Jia, L., Hao, R., Fu, D., 2019. A novel CFD-based method for predicting pressure drop and dust cake distribution of ceramic filter during filtration process at macro-scale. Powder Technol. 353, 27–40. http://dx.doi.org/10.1016/J.POWTEC.2019.05.014.

Mujeebu, M.A., Abdullah, M.Z., Bakar, M.Z., Mohamad, A.A., Abdullah, M.K., 2009. A review of investigations on liquid fuel combustion in porous inert media. Prog. Energy Combust. Sci. 35 (2), 216–230. http://dx.doi.org/10.1016/J.PECS.2008.11.001.

Pfitzner, J., 1976. Poiseuille and his law. Anaesthesia 3 (1), 273–275.

Porvair Filtration Group Ltd, 2021. World Class Filtration Solutions Polymer Filtration Candles, Capsules, Needles, Spinpacks and Disposable Cartridges. Tech. Rep..

Saleh, A.M., Fotovati, S., Vahedi Tafreshi, H., Pourdeyhimi, B., 2014. Modeling service life of pleated filters exposed to poly-dispersed aerosols. Powder Technol. 266, 79–89. http://dx.doi.org/10.1016/j.powtec.2014.06.011.

Sidiropoulou, M.G., Moutsopoulos, K.N., Tsihrintzis, V.A., 2007. Determination of forchheimer equation coefficients a and b. Hydrol. Process. 21 (4), 534–554. http://dx.doi.org/10.1002/hyp.6264.

Taghavijeloudar, M., Park, J., Han, M., Taghavi, A., 2019. A new approach for modeling flux variation in membrane filtration and experimental verification. Water Res. 166, 115027. http://dx.doi.org/10.1016/J.WATRES.2019.115027.

Teitel, M., 2010. Using computational fluid dynamics simulations to determine pressure drops on woven screens. Biosyst. Eng. 105 (2), 172–179. http://dx.doi.org/10.1016/j.biosystemseng.2009.10.005.

Tracey, E.M., Davis, R.H., 1994. Protein Fouling of Track-Etched polycarbonate microfiltration membranes. J. Colloid Interface Sci. 167 (1), 104–116. http://dx.doi.org/10.1006/JCIS.1994.1338.